CO Production From CO_2 via Reverse Water-Gas Shift Reaction Performed in a Chemical Looping Mode: Kinetics on Modified Iron Oxide

Marcus Wenzel[a], N. V. R. Aditya Dharanipragada[c], Vladimir V. Galvita[c], Hilde Poelman[c], Guy B. Marin[c], Liisa Rihko-Struckmann[a], Kai Sundmacher[a,b]

[a]*Max-Planck-Institute for Dynamics of Complex Technical Systems, Sandtorstr. 1, 39106 Magdeburg, Germany*
[b]*Otto-von-Guericke University Magdeburg, Universitätsplatz 2, 39106 Magdeburg, Germany*
[c]*Laboratory for Chemical Technology, Ghent University, Technologiepark 914, B-9052, Ghent, Belgium*

Abstract

Carbon monoxide production from carbon dioxide via isothermal reverse water-gas shift chemical looping (RWGS-CL) is studied with a modified iron oxide oxygen carrier material (80 wt% Fe_2O_3-$Ce_{0.5}Zr_{0.5}O_2$). The material is characterized by TEM, XRD and thermogravimetry at temperatures from 750°C to 850°C and gas mole fractions of H_2 and CO_2 from 0.05 to 0.75, respectively. High temperature and high reactant concentrations favor the oxidation and reduction of the material during repeated redox cycles. The reaction rate of reduction is always faster than that of oxidation applying the same gas concentration of H_2 and CO_2, respectively. The long term stability of the material is investigated with 500 redox cycles in a plug flow reactor. The material shows gradual deactivation lowering the CO yield during the first 100 redox cycles. After that, a steady state CO yield is reached for the next 400 redox cycles. Deactivation is attributed to surface sintering which results in slower reaction kinetics. TG data was used for a kinetic analysis applying the master plot method. The experimental data for oxidation and reduction indicated reaction mechanisms, which are well described by a reaction order and a geometrical contraction model. After parameter estimation, a good agreement between the model and the TG data was achieved with the reaction order and geometrical contraction model for oxidation and reduction, respectively. The RWGS-CL process can be used for sustainable CO production from CO_2 if the energy for the process and for H_2 production is supplied by renewable sources.

Keywords: Reverse Water-Gas Shift, Chemical Looping, CO_2 Reduction, CO Production, Iron Oxide

1. Introduction

The Intergovernmental Panel on Climate Change stated in their most recent report [1] that the human influence on climate change is unequivocal. The rapid rise of anthropologically generated CO_2 within the last decades and its effect on global warming necessitate the development of carbon-neutral processes to close the carbon cycle. However, because of its low reactivity CO_2 has few applications in industry and is often exhausted into the atmosphere. Finding ways to use the massive amounts of CO_2 produced every year makes processes greener and might be economically and environmentally beneficial [2, 3].

In recent years, research on (thermo-)chemical looping processes has increased substantially with chemical looping combustion as the main research area for inherent CO_2 separation and capture. Thermochemical looping has been shown to be a viable process for the production of CO, H_2 or a mixture of both (syngas) by splitting CO_2 or water in a cyclic process applying a solid oxygen storage material (OSM) [4, 22]. It has been estimated that thermochemical processes have the highest present and future sun-to-fuel (STF) efficiency [5] for the conversion of CO_2 from fossil power plants to sustainable fuels. However, temperatures exceeding 1000°C are typically needed for the thermal reduction of the OSM, resulting in energy intensive processes and challenging material handling. Milder conditions can be applied by using reducing agents (e.g. H_2 or CH_4) for the reduction of the material [4]. Introducing H_2 for material reduction leads to the reverse water-gas shift chemical looping (RWGS-CL) process, which was investigated by Galvita *et al.* [6, 7] and Daza *et al.* [8]. It is the chemical looping equivalent of the conventional reverse water-gas shift (RWGS) reaction, in which H_2 and CO_2 react according to equation (1).

$$H_2 + CO_2 \rightleftharpoons H_2O + CO \tag{1}$$

In this work, a mixed oxide of 80 wt% Fe_2O_3 and 20 wt% $Ce_{0.5}Zr_{0.5}O_2$ was used as OSM for RWGS-CL. In a previous study regarding the optimal composition of Fe_2O_3-$Ce_{0.5}Zr_{0.5}O_2$ for H_2 production *via* chemical looping, Galvita *et al.* [9] concluded that a composition of 80 wt% Fe_2O_3 and 20 wt% $Ce_{0.5}Zr_{0.5}O_2$ led to the highest H_2 yield and good material stability. Although $Ce_{0.5}Zr_{0.5}O_2$ did not increase the oxygen capacity of the material, the supporting oxide was found to be of great importance, since it improves the structural properties compared to those of the pure Fe/Fe_3O_4 couple. ZrO_2 is known to increase the micro-structural stability against sintering [10], whereas CeO_2 increases material activity, enhancing the rate of reaction [6].

In the RWGS-CL process, two temporal stages can be identified: the reduction of the modified iron oxide with H_2 and subsequently its re-oxidization with CO_2 which yields the de-

sired product, CO. The simplified reaction scheme (assuming that the support metal oxide, $Ce_{0.5}Zr_{0.5}O_2$, does not participate in the reactions) is given by equations (2) and (3).

$$\text{Reduction:} \quad Fe_3O_4 + 4\,H_2 \rightleftharpoons 3\,Fe + 4\,H_2O \tag{2}$$

$$\text{Oxidation:} \quad 3\,Fe + 4\,CO_2 \rightleftharpoons Fe_3O_4 + 4\,CO \tag{3}$$

Redox reactions are considered to occur between Fe_3O_4 and Fe, since the fully oxidized state, Fe_2O_3, is not achievable by oxidation with CO_2 at the considered reaction conditions.

The main advantage of RWGS-CL compared to conventional RWGS is the inherent gas separation. Therefore, unwanted side reactions (e.g. methanation) are eliminated and product separation is simplified. In contrast to thermochemical looping, the RWGS-CL process can be operated isothermally, eliminating the need for solid-phase heat recuperation, which is crucial for process efficiency and economics [11]. Thus, reactor design and operation is simplified. Additionally, the oxygen storage capacity of the material can be exploited efficiently using H_2. While typical thermochemical cycles make use only of a small range in material non-stoichiometry (e.g. ceria-based) [12], here a much higher difference in oxidation state is achieved between the material's reduced and oxidized state. For the modified iron oxide used in this work (80 wt% Fe_2O_3 and 20 wt% $Ce_{0.5}Zr_{0.5}O_2$), the thermodynamically possible CO yield per cycle is 13.8 mol_{CO}/kg of Fe_3O_4-$Ce_{0.5}Zr_{0.5}O_2$ ($Ce_{0.5}Zr_{0.5}O_2$ is assumed to be inert). This is more than 20 times the amount that can be produced by using cerium oxide. A maximum CO yield of 0.58 mol_{CO}/kg_{CeO_2} is achievable assuming a cycle between CeO_2 and $CeO_{2-\delta}$ with a non-stoichiometry of $\delta = 0.1$. In the literature, CO yields of approximately 0.15 mol_{CO}/kg_{ceria} were reported for ceria [12] and 0.2-1.0 mol_{CO}/kg for state-of-the-art perovskite type materials [13, 14]. All reported values here are normalized to the material mass in the highest achievable oxidation state in the corresponding redox cycle.

Current research on chemical looping is exploring materials with high oxygen capacity and structural stability over repeated cycling, like (doped or undoped) ceria and new types of perovskites, which show very promising results [8, 15, 16]. The modified iron oxide, as used in this work, is inexpensive but lacks structural stability at temperatures above approximately 1000°C. However, since the temperature for RWGS-CL is lower than that of typical thermochemical looping processes, the use of modified iron oxide is justified.

In this work, the effect of repeated cycling on the crystallographic structure of the OSM is investigated *via* TEM and XRD. Further, a kinetic analysis of the modified iron material is provided as a basis for process design and analysis. A systematic methodology is applied to identify a kinetic model for the oxidation and reduction of the material, enabling the mathematical description of the process. Precise kinetic information available in the literature for various materials is still rather limited and often restricted to oxidation kinetics for thermochemical cycles [17, 18, 19, 20]. To the best of our knowledge, there are as of yet no detailed kinetics reported for the RWGS-CL process.

2. Experimental

2.1. Material Synthesis

The Fe_2O_3-$Ce_{0.5}Zr_{0.5}O_2$ samples were synthesized by urea hydrolysis using $Fe(NO_3)_3 \cdot 9H_2O$ (99.0%, Fluka), $Ce(NO_3)_3 \cdot 6H_2O$ (99.0%, Fluka) and $ZrO(NO_3)_3 \cdot 6H_2O$ (99.0%, Fluka). The mixed metal salt solution (0.1 M) was added to a 0.4 M solution of urea (99.0%, Fluka) to yield a salt to urea solution ratio of 2 : 1 (v/v). The precipitate solution was mixed at 100°C for 24 h. After the suspension was cooled to room temperature, the precipitate was separated from the solution. The solid product was washed with ethanol and dried overnight in an oven at 110°C. Finally, the prepared Fe_2O_3-$Ce_{0.5}Zr_{0.5}O_2$ was calcinated at 800°C.

Since the synthesized, finely powdered material was unsuitable for a plug flow reactor (large pressure drop, high tendency towards sintering), the material was pelletized, crushed and sieved to obtain particles of a defined size between 260 and 520 µm.

2.2. Material Pretreatment and Stabilization

The aim of the experiments was to obtain kinetic information about the material. It is well known that the activity of oxygen storage materials decreases over repeated redox cycles [15, 21]. The deactivation mainly occurs due to sintering of the particles and changes in their crystallographic structure. Thus, it can be expected that kinetic measurements with as-prepared material will not yield representative results. Therefore, the material sample was exposed first to repeated redox cycles to stabilize its structure before thermogravimetric experiments were conducted.

For material stabilization, a sample of 250 mg was fixed inside a quartz reactor with glass wool. The reactor was placed in an oven and heated to the reaction temperature (800°C) under inert atmosphere. The gas composition was then repeatedly switched between a mole fraction of $x_i = 0.5$ of either H_2 (material reduction) or CO_2 (material oxidation) balanced with He as inert gas. The reaction time for reduction and oxidation was 5 min with 3 min of inert gas flushing (He) between the steps, which were repeated until 500 cycles were reached. During the pretreatment, the outlet gas composition was followed by mass spectrometry (Agilent 5973Network MSD) to obtain information about material activity over repeated redox cycles.

2.3. TEM

A morphological and local elemental analysis was carried out in a microscope JEOL JEM-2200FS, Cs-corrected, operated at 200 kV and equipped with a Schottky-type field-emission gun (FEG) and EDX JEOL JED-2300D. Samples were prepared by immersion of a lacey carbon film on a copper support grid into the powder. Particles sticking to the carbon film were investigated. A beryllium sample retainer was used to eliminate secondary X-ray fluorescence in EDX spectra originating from the sample holder.

2.4. Conventional and in situ XRD

The crystallographic changes in the sample were followed in a homebuilt Bruker-AXS D8 Discover apparatus (Cu Kα radiation of 0.154 nm). The reactor consisted of a stainless steel chamber with Kapton window to allow X-ray transmission. The sample was uniformly spread on a Si wafer and no interaction of sample with Si wafer was observed during the reaction. The diffraction data were recorded using a linear Vantec detector which allowed capturing diffracted X-rays in a 20° window with an angular resolution of 0.1°. The reactor chamber was evacuated to a base pressure of 4 Pa by a rotation pump before reaction. Gases were supplied to the reactor chamber from a rig with calibrated mass-flow meters. H_2 (x_{H_2} = 0.05 in He) was used as reducing gas, CO_2 (x_{CO_2} = 0.3 in He) for oxidation and pure He for purging the reactor. The in situ experiment was performed at a temperature of 800°C. After heating to the reaction temperature in He, the sample was monitored with in situ XRD during isothermal cycling.

2.5. Thermogravimetric Analysis

The mass change of 100 mg of the stabilized sample was recorded under alternating gas composition in a thermogravimetric analyzer (Mettler Toledo TGA/SDTA 851e). The sample was placed in a cylindrical sample holder and a constant gas flow rate of 100 ml/min was applied in all experiments. Additionally, a constant flow of 20 ml/min of He was added to protect the precision balance from reactive gas. Therefore, the total gas flow rate was 120 ml/min. For the reduction and oxidization steps, H_2 and CO_2 were used in varying concentrations, respectively, balanced with He as inert gas.

The sample was heated to the desired temperature in the TG unit with a constant rate of 20 °C/min under an inert atmosphere (He). Then, reactive gas was applied under isothermal conditions. At first, a reducing environment was established with H_2, ensuring that the sample was completely reduced to Fe. The next 45 min an oxidizing environment (CO_2) was applied to re-oxidize the sample to Fe_3O_4. This was followed by 45 min of reduction with H_2. At last, the sample was cooled to ambient conditions with a constant rate of 10 °C/min.

The outlet gas composition was analyzed by mass spectrometry (Pfeiffer Vacuum GSD320) to assure that no other gaseous substances were produced.

Blank runs were conducted without sample before each experiment to account for buoyancy effects. The mass change without sample was subtracted from the experiment with sample. Thus, the recorded mass change is only attributable to the mass change of the sample. The same sample was used in all the experiments with various gas concentrations and temperatures.

Preliminary experiments showed that reaction rates drop at temperatures below 750°C. Conversely, at temperatures exceeding 850°C, the material's structure collapsed due to sintering up to the point of surface melting (not shown) which led to severely decreased activity . Measurements were conducted at temperatures 750, 800 and 850°C and reactive gas mole fractions of 0.08, 0.25, 0.5 and 0.75. Due to the slow rate of reaction, the experiment with a reactive gas mole fraction of 0.08 at 750°C was omitted. Therefore, 11 TG experiments were conducted in total.

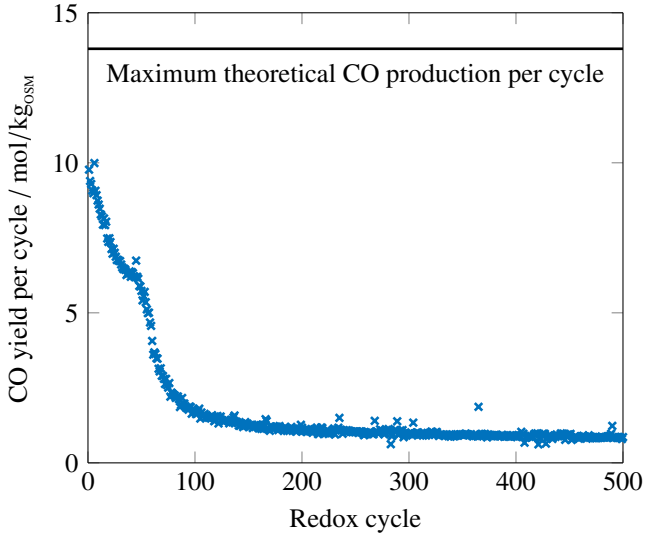

Figure 1: CO yield per cycle for 500 redox cycles at 800°C with a reactive gas mole fraction of 0.5 for CO_2 and H_2 in He, respectively. OSM refers to the oxidized material (Fe_3O_4-$Ce_{0.5}Zr_{0.5}O_2$). Reaction times for oxidation and reduction were 5 min each with 3 min inert gas (He) flushing between. The CO yield per cycle decreases gradually during the first 100 cycles, then reaches a steady state.

3. Results and Discussion

3.1. Material Pretreatment

The CO production per cycle during the stabilization treatment is shown in Figure 1. In the first cycle, ≈ 72% of the theoretically possible amount of CO was obtained. After the gradual deactivation of the material during the first 100 cycles, a steady CO yield was achieved for the next 400 cycles, yielding a stable CO yield of approximately 1.0 mol/kg$_{OSM}$ per redox cycle. Even though only a fraction of the theoretically possible value was achieved, the measured CO production per cycle in steady state is comparable to the numbers reported by other research groups with more advanced materials (e.g. perovskites) at temperatures well above 1000°C [12, 13] (see also section 1). The long time stability and the reaction kinetics of the oxygen storage material may be further improved by nanostructuring as recently demonstrated by Gao *et al.* [22].

3.2. TEM

The HR-TEM images of the as-prepared and 500 times cycled sample are displayed in Figure 2 and 3. The TEM micrograph for the as-prepared material (Figure 2a) shows the presence of particles (~ 35 − 50 nm) with similar morphology. The elemental composition of this material was identified by means of EDX mapping, showing the presence of Fe (red), Ce (green) and Zr (blue) (Figure 2b). Zr is distributed throughout the sample (Figure 2c), as is Fe (not shown), whereas strong clustering of Ce (Figure 2d) is observed. Prolonged cycling of the sample results in increased particle sizes (Figure 3) due to sintering.

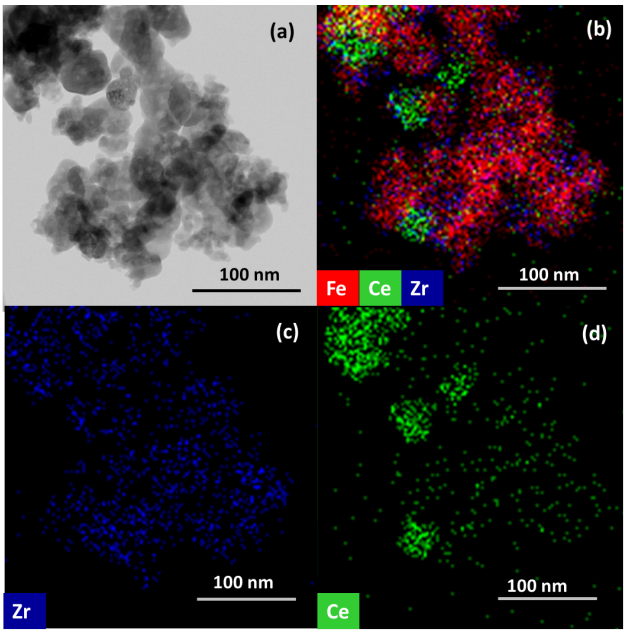

Figure 2: HR-TEM image of as-prepared Fe_2O_3-$Ce_{0.5}Zr_{0.5}O_2$ showing (a) the sample morphology; (b) the EDX mapping of the constituent elements (Fe, Ce, Zr) along with the individual elemental maps of (c) Zr and (d) Ce.

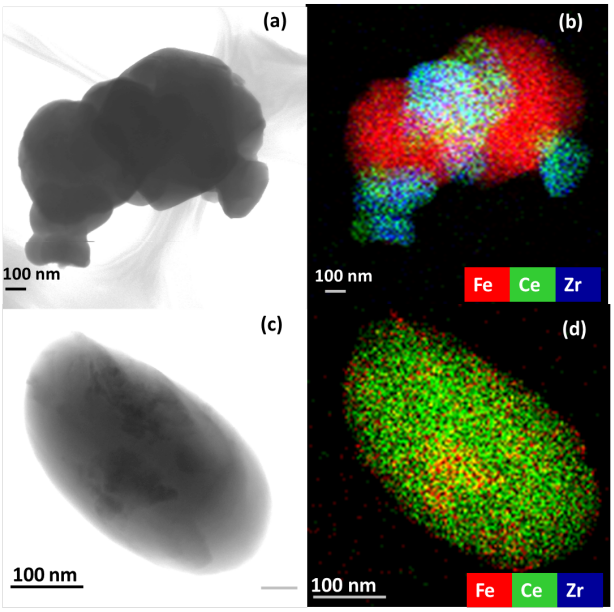

Figure 3: The TEM micrograph of a 500 times cycled sample with different morphologies. (a) Morphology with separated particles (b) EDX mapping of Fe, Ce, Zr. (c) Morphology with embedded structure, and (d) the EDX mapping showing the distribution of constituent elements.

However, this phenomenon led to an evolution into two particles with different morphologies. In the first type (Figure 3a), very large particles are observed (~ 200 – 600 nm), consisting of segregated Fe rich and Ce-Zr rich phases, based on the EDX overlay of images (Figure 3b). Compared to the as-prepared sample (Figure 2b), the distribution of Ce is more uniform in the Ce-Zr rich phase. In the second type of morphology (Figure 3c) small particles (~ 100 nm) are incorporated inside relatively large particles (~ 300 nm). The EDX mapping (Figure 3d) reveals Ce and Zr are both spread out throughout the large particles, while Fe is located in smaller particles inside the Ce-Zr phase.

3.3. XRD Analysis

The crystalline phases in as-prepared and 500 times cycled Fe_2O_3-$Ce_{0.5}Zr_{0.5}O_2$ were identified using XRD (Figure 4). The as-prepared materials (Figure 4a) show diffraction peaks corresponding to Fe_2O_3 (33.15°, 35.61°, 40.85°, 49.48°, 54.09°, PDF: 00-033-0664), CeO_2 (28.55°, 33.08°, 47.47°, 56.33°, PDF: 00-033-0394) and $Ce_{0.5}Zr_{0.5}O_2$ (29.10°, 33.70°, 48.50°, 57.50°, PDF: 00-038-1439) phases. The diffraction pattern of Fe_2O_3 is clearly identified, whereas CeO_2 and $Ce_{0.5}Zr_{0.5}O_2$ show a close overlap of peak positions. However, the presence of separate CeO_2 and $Ce_{0.5}Zr_{0.5}O_2$ phases can be discerned from the diffraction peaks at higher angles (~ 48° and ~ 57°) where they are relatively well resolved in comparison to lower angles (~ 29° and ~ 33°). The lattice parameter calculated from the overall peak at ~ 29° yielded a value of 0.5361 nm, which is intermediate to $Ce_{0.5}Zr_{0.5}O_2$ (0.5301 nm) and pure CeO_2 (0.5410 nm). Based on the resolved diffractions at higher angle, it is likely that this low angle diffraction equally contains contributions from CeO_2 and $Ce_{0.5}Zr_{0.5}O_2$. The TEM images reveal homogeneous distribution of Zr with strong clustering of Ce (Figure 2c and 2d). The results from TEM and XRD hence imply the existence of Ce in solid solution between Ce and Zr, present throughout the sample, and in separate dispersed CeO_2 clusters, next to the Fe_2O_3 phase. On the other hand, no separate diffraction peaks of ZrO_2 were identified. Similarly, in the 500 times cycled sample (Figure 4b), phases of Fe_3O_4 (30.10°, 35.45°, 47.17°, 43.09°, 53.45°, 56.98°, PDF: 03-065-3107) along with $Ce_{0.5}Zr_{0.5}O_2$ are identified. Unlike the as-prepared sample no diffraction peaks pertaining to Fe_2O_3 and CeO_2 are present. Reoxidation of reduced material with CO_2 results in the formation of Fe_3O_4, instead of Fe_2O_3, which can only be obtained by using oxygen/air as re-oxidizing agent [23]. No peaks or shoulders typical for pure CeO_2 are noticed. Further, the lattice parameter calculation for the peak at ~ 29° exhibits a value of 0.5312 nm indicating a solid solution between Ce and Zr. Hence the XRD patterns represent a mixed Ce-Zr phase in line with the TEM images (Figure 3) where Ce and Zr are more evenly distributed in comparison to the as-prepared sample.

In situ XRD for one complete redox cycle is depicted in Figure 5. At the start of the experiment, only Fe_3O_4 is detected in He atmosphere. At 2.5 min, the gas mole fraction of H_2 was switched to 0.05 H_2 in He, resulting in a reducing environment, in which Fe_3O_4 was first converted into FeO and then into Fe. At t = 17.5 min an oxidizing environment was established with x_{CO_2} = 0.3 in He. Again, FeO is formed in an intermediate step, which reacts further to Fe_3O_4. The results indicate that under the investigated conditions full conversion for reduction and oxidation is achieved according to equations (2) and (3).

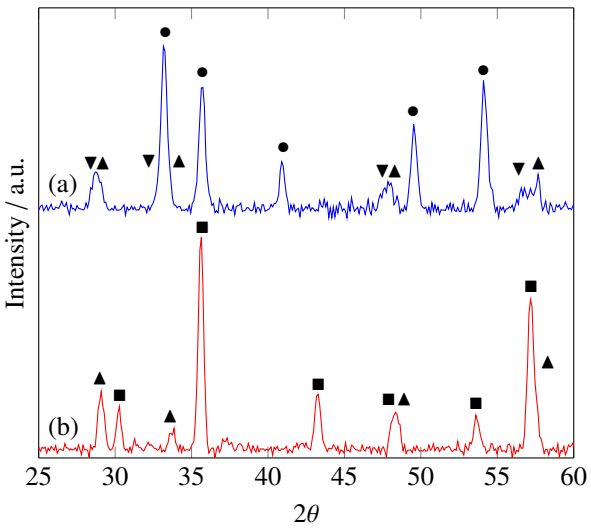

Figure 4: XRD patterns of (a) as-prepared and (b) 500 times cycled Fe_2O_3-$Ce_{0.5}Zr_{0.5}O_2$. (•) Fe_2O_3, (■) Fe_3O_4, (▲) $Ce_{0.5}Zr_{0.5}O_2$ and (▼) CeO_2.

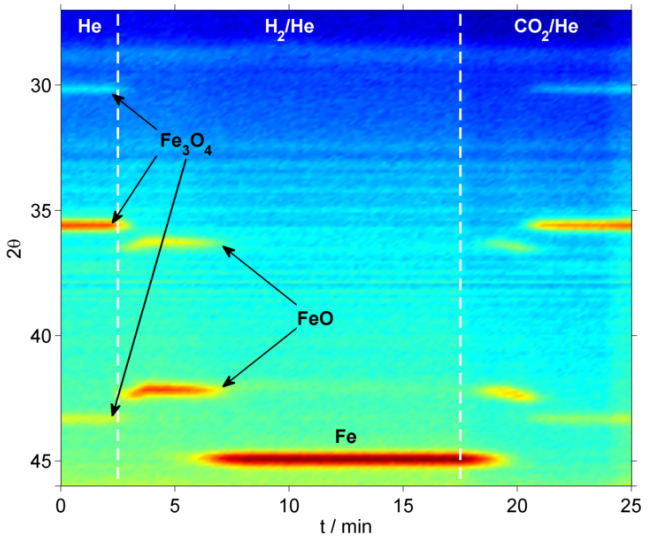

Figure 5: In situ XRD for one full redox cycle at 800°C and a total gas flow of 1 l/min. Fe_3O_4 is reduced to Fe with H_2 and re-oxidized to its initial state with CO_2. In both transitions, the presence of FeO is detected, which is formed in an intermediate step. Both reduction and oxidation yield to full conversion, as described in equations (2) and (3).

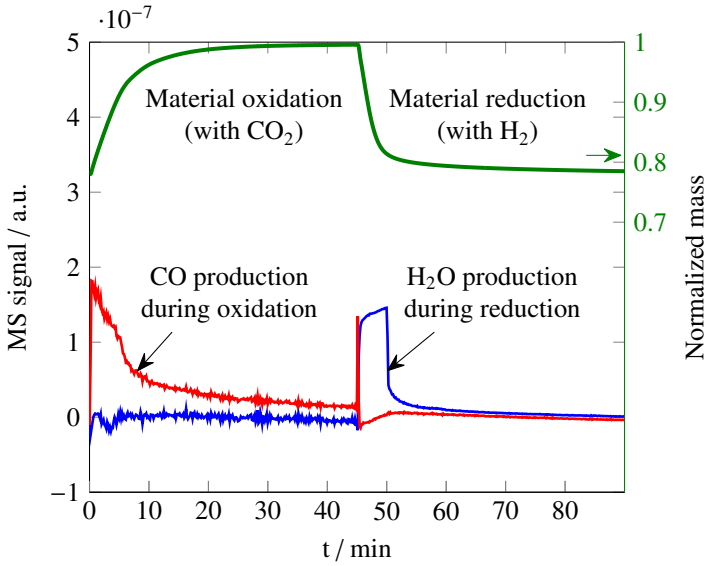

Figure 6: Thermogravimetry results for stabilized OSM (green, right axis) at 800°C and a reactive gas mole fraction of 0.75 for CO_2 (oxidation) and H_2 (reduction) balanced with He together with mass spectrometry signal of the corresponding outlet gas (left axis). The MS signal was corrected by subtracting the measured signal from the blank run without OSM in the TG unit. The red and blue lines indicate the MS signal for CO and H_2O, respectively.

3.4. Thermogravimetric Analysis

In Figure 6, TG data of the stabilized OSM is shown together with the MS signal of the outlet gas composition during oxidation and reduction at 800°C with reactive gas mole fractions of 0.75 for both CO_2 and H_2. The production of CO during oxidation and water formation during reduction of the material was observed according to equations (3) and (2). No other substances were detected apart from the reactants. The rate of CO production is directly coupled with the material oxidation according to equation (3). Initially,CO yield is high and then gradually decreases until the material is fully oxidized.

The mass change of the stabilized OSM under different conditions is shown in Figure 7 for oxidation (left) and reduction (right). The measured mass of the sample was normalized to the mass of the sample in its oxidized state (1.00 for Fe_3O_4-$Ce_{0.5}Zr_{0.5}O_2$). In the experiments, a normalized mass of approximately 0.78 was measured initially, which is very close the theoretical normalized value of 0.779 for the reduced state Fe-$Ce_{0.5}Zr_{0.5}O_2$ (assuming $Ce_{0.5}Zr_{0.5}O_2$ is not reduced). This indicates that the mass change upon reduction is likely due to the reduction of iron oxide only and $Ce_{0.5}Zr_{0.5}O_2$ is not reduced. If it is assumed that $Ce_{0.5}Zr_{0.5}O_2$ is reduced to $Ce_{0.5}Zr_{0.5}O$, slightly lower values of 0.765 could be obtained theoretically. Upon oxidation, values of approximately 1.00 are reached (in some experiments, the reaction rates for oxidation were too slow to reach the final oxidation state). Overall, the reaction rates of oxidation and reduction increase as a function of temperature and concentration of reactive gas, while the rate of reduction is higher than that of oxidation. Even at low gas concentration of $x_{H_2} = 0.08$, the reduction at 800°C leads to complete conversion within 25 min, while during oxidation the material is still not fully oxidized after 45 min.

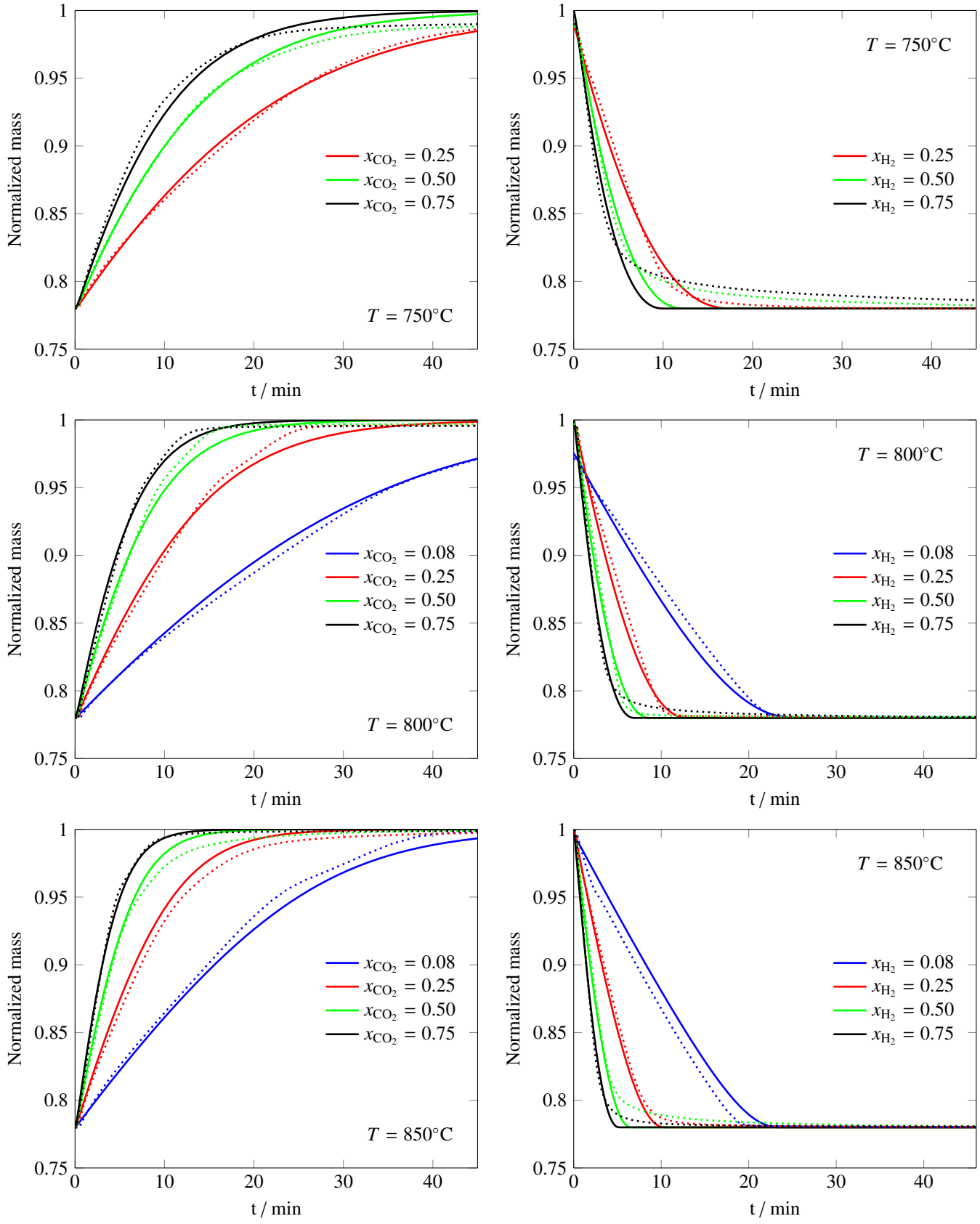

Figure 7: Thermogravimetry results for stabilized OSM (dotted lines) and simulated model (solid lines) for oxidation (left, R2 model) and reduction (right, R2 model) at 750, 800 and 850°C. Different colors indicate the corresponding mole fractions of CO_2 and H_2 (balanced with He), respectively. The mass is normalized with the mass of the oxidized sample (Fe_3O_4-$Ce_{0.5}Zr_{0.5}O_2$).

Even though the material showed deactivation during 500 redox cycles in the stabilization pretreatment (see Figure 1), the mass change of the material in the subsequent TG experiments indicates that the material is cycled between Fe and Fe_3O_4 according to equations (2) and (3). The observed deactivation during the pretreatment obviously did not influence the attainable oxidation states of the material in TG experiments. The observed decline of CO yield during the material pretreatment (see Figure 1) is likely explained by reduced rate of reactions due to sintering. During oxidation and/or reduction the material is not completely converted within the limited reaction time in the plug flow reactor.

3.5. Master Plot Analysis

The rate equations for various reaction mechanisms were compared to the experimental TG data by master plot analysis [24]. This graphical method allows to deduce and compare kinetic models with the experimental data without prior identification of the kinetic parameters of the rate equations. Thus, a qualitative indication about the reaction mechanism is obtained and possible erroneous conclusions due to weakly identified parameters can be avoided. Finally, the parameter estimation can be done only for the most probable model instead of for numerous models.

To apply the method, the generalized solid-state kinetic rate expression

$$\frac{\mathrm{d}\alpha}{\mathrm{d}t} = k^0 \exp\left(-\frac{E_A}{RT}\right) f(\alpha) f(x_i) \tag{4}$$

is used, where α is the reaction extent at time t, $f(\alpha)$ a function depending on the reaction mechanism, $f(x_i)$ a function of the reactive gas mole fraction x_i, E_A the activation energy, k^0 the pre-exponential factor of Arrhenius, and T the absolute temperature. By introducing the generalized time, Θ (reaction time to attain a certain α at any temperature), defined as

$$\Theta = \int_0^t \exp\left(-\frac{E_A}{RT}\right) \mathrm{d}t \tag{5}$$

the kinetic rate expression at any temperature can be derived by differentiation of eq. (5)

$$\frac{\mathrm{d}\Theta}{\mathrm{d}t} = \exp\left(-\frac{E_A}{RT}\right) \tag{6}$$

The combination of eq. (4) and (6) yields

$$\frac{\mathrm{d}\alpha}{\mathrm{d}\Theta} = k^0 f(\alpha) f(x_i) \tag{7}$$

Using a reference point at $\alpha = 0.5$, the following equation is derived from eq. (7)

$$\frac{\mathrm{d}\alpha/\mathrm{d}\Theta}{(\mathrm{d}\alpha/\mathrm{d}\Theta)_{\alpha=0.5}} = \frac{f(\alpha)}{f(0.5)} \tag{8}$$

Being only dependent on α, eq. (8) compares the experimental data (left-hand side) with the suggested model (right-hand side). Both sides are equal when the chosen model exactly describes all experimental data points. Thus, by plotting the experimental data against various theoretical models according to eq. (8), one obtains a graphical way to choose a suitable model without determination of the kinetic parameters.

Table 1: Used gas-solid kinetic equations for master-plot analysis, adapted from Heidebrecht *et al.* [26].

Name	$f(\alpha)$
Contracting Cylinder (R2)	$(1-\alpha)^{1/2}$
Contracting Sphere (R3)	$(1-\alpha)^{2/3}$
Reaction Order (Fn)	$(1-\alpha)^n$
Power Law (Pn)	α^n
Avrami-Erofeev (A2)	$(1-\alpha)[-\log(1-\alpha)]^{1/2}$
Avrami-Erofeev (A3)	$(1-\alpha)[-\log(1-\alpha)]^{2/3}$
Avrami-Erofeev (A4)	$(1-\alpha)[-\log(1-\alpha)]^{3/4}$
1D Diffusion (D1)	$(1-\alpha)^0(1-(1-\alpha)^1)^{-1}$
2D Diffusion (D2)	$(1-\alpha)^{1/2}(1-(1-\alpha)^{1/2})^{-1}$
3D Diffusion (D3)	$(1-\alpha)^{2/3}(1-(1-\alpha)^{1/3})^{-1}$

A list of the common kinetic functions for gas-solid reactions is given in Table 1. The gas-solid reaction kinetics considered here are categorized in the geometrical contraction (Rn), the reaction order (Fn), the nucleation (Pn and An) and the diffusion groups (Dn), where n is the reaction order. For geometrical contraction models (Rn), a rapid nucleation is assumed and the rate is dependent on the progress of the reaction interface towards to the crystal center. Reaction order models (Fn) are based on homogeneous mechanistic assumptions. Power law models (Pn) are applicable for reactions where the formation and growth of nuclei are rate limiting. Avrami-Erofeev models (An) include further restrictions on nuclei growth like coalescence and ingestion. Thus, they yield s-shaped curves which account for a restricted rate of reaction in the final stage. Diffusion models (Dn) are used to describe reactions where the rate is controlled by the limited diffusion of reactants or products to or from the reaction interface. Khawam *et al.* provided a detailed discussion about the theoretical foundations of solid-state reaction kinetics [25].

Figure 8 shows the master plots for the experimental data (eq. (8), l.h.s.) together with theoretical models (eq. (8), r.h.s.) from Table 1 for oxidation (Figure 8a) and reduction (Figure 8b). For clarity, not all theoretical models were plotted but only representative ones from each model category. While all points coincide at the reference point of $\alpha = 0.5$, they disperse clearly in the range of $\alpha < 0.5$, allowing for model discrimination.

For oxidation (Figure 8a), most of the experimental points are located between the geometrical contraction model (R2) and the reaction order model (F2). We chose the R2 model as the most appropriate kinetic model to describe the material oxidation. However, by comparing the R and F models, one observes that they are mathematically very similar and only differ in their respective exponents. Thus, the exponent n_o is estimated in section 3.6 to allow for more flexibility and to minimize the deviation between model simulation and experimental data.

For the reduction stage, a different behavior was observed for experiments with $x_{H_2} = 0.75$ and for experiments with gas mole fraction of $x_{H_2} = 0.5$ at temperatures of 750 and 850°C.

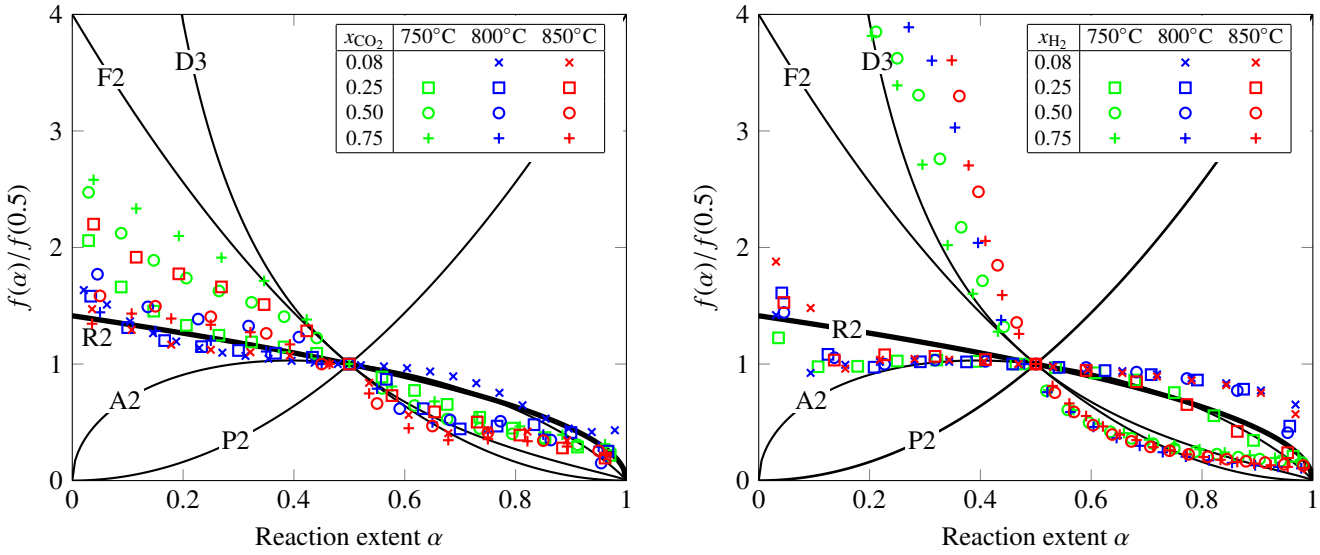

(a) Oxidation

(b) Reduction

Figure 8: Master plot results for oxidation (8a) and reduction (8b). Experimental results shown as markers, theoretical models as lines with their respective abbreviations (see Table 1). Thick lines indicate the chosen models for oxidation and reduction, respectively.

The data of these experiments correlate better with a diffusion limited reaction model (D3). This behavior was observed only for reduction. However, similarly to oxidation most experimental observations for reduction are well described by the R2 model. The exponent n_R of the R2 model for the reduction was estimated together with all other parameters as discussed in the following section.

3.6. Parameter Estimation

Master plot analysis showed that kinetic models of the geometrical contraction group (the R2 model in particular) are most appropriate to describe the kinetic behavior of material oxidation and reduction. Since the observed mass change in TG experiments indicated that $Ce_{0.5}Zr_{0.5}O_2$ is not participating in the redox reactions, a mathematical model was derived based only on the oxidation and reduction of iron oxide (see equations (3) and (2), respectively). The intermediate step through FeO was not explicitly modeled as the reactions from Fe to FeO and from FeO to Fe_3O_4 (and *vice versa*) seem to proceed at a very similar rate. Therefore, the TG data the did not allow for a clear discrimination between the reaction steps. The proposed model follows an engineering approach and provides a trade-off between simplicity and accuracy. Using the R2 model, the reaction rates for oxidation and reduction are described by equations (9) and (10), respectively.

$$r_O = k_O^0 \exp\left(-\frac{E_{A,O}}{RT}\right)\left(1 - x_{\mathrm{FeO_{4/3}}}\right)^{n_O} x_{\mathrm{CO_2}}^{m_O} \tag{9}$$

$$r_R = k_R^0 \exp\left(-\frac{E_{A,R}}{RT}\right)\left(1 - x_{\mathrm{Fe}}\right)^{n_R} x_{\mathrm{H_2}}^{m_R} \tag{10}$$

Here, k^0, E_A, n and m are adjustable parameters for oxidation (index O) and reduction (index R), adding up to a total of eight parameters. For modeling details, see Appendix A.

Table 2: Estimated kinetic parameters and 95% confidence intervals for oxidation and reduction reaction described by equations (9) and (10), respectively. Parameters valid from 750 to 850°C with reactive gas mole fractions x_{H_2,CO_2} from 0.08 to 0.75. OSM refers to the material in its oxidized state Fe_3O_4-$Ce_{0.5}Zr_{0.5}O_2$.

Estimated parameter	Oxidation	Reduction
n	1.002 ± 0.004	0.724 ± 0.008
m	0.618 ± 0.002	0.461 ± 0.004
k^0 / mol/kg$_{\mathrm{OSM}}$/s	18199 ± 827	1140 ± 125
E_A / kJ/mol	111.6 ± 0.4	80.7 ± 0.9
R^2	0.9930	0.9827

Parameter estimation was done with the statistics toolbox in MATLAB. The nonlinear least-squares regression function *nlinfit* was used for parameter estimation. The confidence intervals were calculated with the function *nlparci* and the coefficient of determination R^2 was determined by the following equation

$$R^2 = 1 - \frac{\sum_i (y_i - f_i)^2}{\sum_i (y_i - \bar{y}_i)^2}, \tag{11}$$

where y_i are the experimental observations and f_i are the predicted values from the model at each point i. The mean of the experimental points is denoted by $\bar{y}_i$.

The estimates for all kinetic parameters are given in Table 2. In Figure 7, the gravimetric data (dotted line) are shown together with the model prediction (solid line) for the different experimental conditions. For oxidation, the model simulates the data very well, which is reflected in a high R^2 value of 0.9930. For the reduction, slight deviations of the model prediction from the experimental data are observed for the experiments with gas mole fractions of $x_{H_2} \geq 0.5$, as discussed

in section 3.5. The deviations are more pronounced in the later stages of the reduction (see Figure 7). Here, the model predicts a slightly higher reaction rate than observed in the experiments. However, a value of $R^2 = 0.9827$ for the reduction indicates an acceptable agreement between model and experimental data.

The estimated value of $n_o = 1.002$ confirms the previous conclusion from master plot analysis, that the reaction order for the oxidation lies between the Rn and Fn group. However, the value indicates that the F1 model is most appropriate for the description of material oxidation. For reduction, the estimated value of $n_R = 0.724$ corresponds closely to the R3 model. The narrow confidence intervals for oxidation and reduction confirm a good correlation of the experimental data with the proposed models. The slightly larger confidence interval for k_R^0 ($\pm 11.01\,\%$) indicates that part of the experimental data for material reduction is weakly described by the model.

The reaction orders (m_i) for the gas concentrations are lower than one, indicating that the reaction rates increase only moderately for increasing reactive gas mole fractions. This is also observed experimentally. In Figure 7, the increase of the reaction rates from reactive gas mole fractions of 0.25 to 0.5 is larger than that from 0.5 to 0.75 at all temperatures. This phenomenon is more pronounced in material reduction.

4. Conclusions

The redox behavior of modified iron oxide (80 wt% Fe_2O_3-$Ce_{0.5}Zr_{0.5}O_2$) was investigated for the RWGS-CL process. The material was stabilized for 500 redox cycles. Deactivation takes place during the first 100 cycles. For the remaining 400 cycles, a steady CO yield per cycle was achieved. Repeated cycling led to increased crystallite sizes due to sintering and a phase segregation into Fe rich and Ce-Zr rich phases in the sample. Surface sintering is likely to be the main cause for material deactivation as it leads to slower reaction kinetics and a lower CO yield within a fixed time. The stabilization pretreatment using repeated cycling did not influence the attainable oxidation states of the material as was evidenced by the observed mass change in TG experiments, which closely matched the theoretically possible mass change according to equations (2) and (3). The kinetics for material oxidation with CO_2 and reduction with H_2 were studied by means of TG experiments. The reaction rates of reduction are always faster than those for oxidation under equivalent conditions. Low reaction rates ($T \leq 750°C$) and material instability ($T > 850°C$) limited the temperature range for TG experiments. CO was generated during material oxidation and no other substances were formed. The experimental data were modeled and kinetic parameters were estimated. Oxidation and reduction were best described by a reaction order model and a geometrical contraction model, respectively. The model presented here can be used for further analysis and design of the process as well as for comparison of RWGS-CL to other chemical looping processes.

Acknowledgement

This work was supported by the Long Term Structural Methusalem Funding of the Flemish Government, the Interuniversity Attraction Poles Programme, IAP7/5, Belgian State Belgian Science Policy and the Fund for Scientific Research Flanders (FWO-Vlaanderen project G004613N). The authors also thank G. Rampelberg and C. Detavernier for the use of in situ XRD (Department of Solid State Sciences, Ghent University) and L. Buelens for his technical support concerning STEM analysis.

Appendix A. Modeling

Appendix A.1. Balance Equations

For the ease of modeling, equations 3 and 2 were normalized so that the oxidized state of iron oxide has one iron atom. Thus, the considered reactions for oxidation and reduction are given by equations (A.1) and (A.2), respectively.

$$\text{Oxidation:} \quad \mathrm{Fe} + 4/3\,\mathrm{CO_2} \rightleftharpoons \mathrm{FeO_{4/3}} + 4/3\,\mathrm{CO} \tag{A.1}$$

$$\text{Reduction:} \quad \mathrm{FeO_{4/3}} + 4/3\,\mathrm{H_2} \rightleftharpoons \mathrm{Fe} + 4/3\,\mathrm{H_2O} \tag{A.2}$$

The mole balances used to describe the TG unit are given in terms of mole fractions for the gas (x_i) and solid phase (x_j) according to equations (A.3) and (A.4).

$$\frac{\mathrm{d}x_i}{\mathrm{d}t} = \frac{\dot{F}}{V_{\mathrm{TG}}}\left(x_i^{(in)} - x_i\right) + \frac{m_{\mathrm{OSM}}}{c_{t,g}V_{\mathrm{TG}}}\nu_{i,k}r_k \tag{A.3}$$

$$\text{with } i = \{\mathrm{CO}, \mathrm{CO_2}, \mathrm{H_2}, \mathrm{H_2O}\}$$

$$\frac{\mathrm{d}x_j}{\mathrm{d}t} = M_{\mathrm{OSM}}\nu_{j,k}r_k \tag{A.4}$$

$$\text{with } j = \{\mathrm{Fe}, \mathrm{FeO_{4/3}}\}$$

Here, index $k = \{O, R\}$ for oxidation (eq. (A.1)) and reduction (eq. (A.2)), respectively. $\dot{F}$ is the total gas flow rate, which was 120 ml/min for all experiments and V_{TG} is the volume of the thermogravimetry unit (38 ml). The mole fractions of the inlet gas stream are denoted by $x_i^{(in)}$. The total gas concentration, $c_{t,g}$, is calculated from the ideal gas law according to

$$c_{t,g} = \frac{p}{RT}, \tag{A.5}$$

where R is the universal gas constant and p and T are the system pressure and temperature, respectively. Since the process is operated at high temperature and ambient pressure, the use of the ideal gas law is justified. The mass m_{OSM} and the molar mass M_{OSM} of the OSM at each point in time can be calculated by equations (A.6) and (A.7).

$$m_{\mathrm{OSM}} = w_{\mathrm{Fe}}m_{\mathrm{Fe}} + w_{\mathrm{FeO_{4/3}}}m_{\mathrm{FeO_{4/3}}} \tag{A.6}$$

$$M_{\mathrm{OSM}} = x_{\mathrm{Fe}}M_{\mathrm{Fe}} + x_{\mathrm{FeO_{4/3}}}M_{\mathrm{FeO_{4/3}}} \tag{A.7}$$

Here, w denotes the mass fraction, which can be calculated from the mole fractions by

$$w_j = \frac{x_j M_j}{\sum_j x_j M_j}. \tag{A.8}$$

Appendix A.2. Kinetics

The reaction rates for oxidation and reduction are described by the following equations, respectively

$$r_O = k_O f(\alpha_O) x_{CO_2}^{m_O} \tag{A.9}$$

$$r_R = k_R f(\alpha_R) x_{H_2}^{m_R}, \tag{A.10}$$

where k_O and k_R are the kinetic constants. Their temperature dependency is described by the Arrhenius equation:

$$k = k^0 \exp\left(-\frac{E_A}{RT}\right) \tag{A.11}$$

The function $f(\alpha)$ for the reaction extent of oxidation and reduction is depending on the reaction model used (see Table 1). The reaction extent is equivalent to the solid mole fraction, since only two different solid states are distinguished. Thus, the reaction extents for oxidation (α_O) and reduction (α_R) are equal to $x_{FeO_{4/3}}$ and x_{Fe}, respectively. The influence of the reactive gas mole fraction is described by $x_{CO_2}^{m_O}$ and $x_{H_2}^{m_R}$. The reaction rates are, therefore, functions of the temperature T, the reaction extent α, and the reactive gas mole fractions x_{H_2} and x_{CO_2}.

References

[1] IPCC, Climate Change 2013: The Physical Science Basis. Working Group I Contribution to the Fifth Assessment Report of the Intergovernmental Panel on Climate Change, Cambridge University Press (2014).

[2] J. Kim, C. A. Henao, T. A. Johnson, D. E. Dedrick, J. E. Miller, E. B. Stechel, C. T. Maravelias, Methanol Production From CO_2 Using Solar-Thermal Energy: Process Development and Techno-Economic Analysis, Energy Environ. Sci. 4 (2011) 3122 – 3132.

[3] J. Kim, T. A. Johnson, J. E. Miller, E. B. Stechel, C. T. Maravelias, Fuel Production From CO_2 Using Solar-Thermal Energy: System Level Analysis, Energy Environ. Sci. 5 (2012) 8417 – 8429.

[4] C. Agrafiotis, M. Roeb, C. Sattler, A Review on Solar Thermal Syngas Production via Redox Pair-Based Water/Carbon Dioxide Splitting Thermochemical Cycles, Renewable and Sustainable Energy Reviews 42 (2015) 254 – 285.

[5] D. S. Mallapragada, N. R. Singh, V. Curteanu, R. Agrawal, Sun-to-Fuel Assessment of Routes for Fixing CO_2 as Liquid Fuel, Industrial & Engineering Chemistry Research 52 (2013) 5136 – 5144.

[6] V. V. Galvita, H. Poelman, V. Bliznuk, C. Detavernier, G. B. Marin, CeO_2-Modified Fe_2O_3 for CO_2 Utilization via Chemical Looping, Industrial & Engineering Chemistry Research 52 (2013) 8416 – 8426.

[7] L. K. Rihko-Struckmann, P. Datta, M. Wenzel, K. Sundmacher, N. V. R. A. Dharanipragada, H. Poelman, V. V. Galvita, G. B. Marin, Hydrogen and Carbon Monoxide Production by Chemical Looping over Iron-Aluminium Oxides, ENERGY TECHNOLOGY 4 (2016) 304–313.

[8] Y. A. Daza, R. A. Kent, M. M. Yung, J. N. Kuhn, Carbon Dioxide Conversion by Reverse Water-Gas Shift Chemical Looping on Perovskite-Type Oxides, Industrial & Engineering Chemistry Research 53 (2014) 5828 – 5837.

[9] V. V. Galvita, T. Hempel, H. Lorenz, L. K. Rihko-Struckmann, K. Sundmacher, Deactivation of Modified Iron Oxide Materials in the Cyclic Water Gas Shift Process for CO-Free Hydrogen Production, Industrial & Engineering Chemistry Research 47 (2008) 303 – 310.

[10] T. Kodama, Y. Nakamuro, T. Mizuno, A Two-Step Thermochemical Water Splitting by Iron-Oxide on Stabilized Zirconia, Journal of Solar Energy Engineering 128 (2006) 3–7. International Solar Energy Conference, Portland, OR, JUL 01-14, 2004.

[11] R. Bader, L. J. Venstrom, J. H. Davidson, W. Lipiński, Thermodynamic Analysis of Isothermal Redox Cycling of Ceria for Solar Fuel Production, Energy & Fuels 27 (2013) 5533 – 5544.

[12] P. Furler, J. R. Scheffe, A. Steinfeld, Syngas Production by Simultaneous Splitting of H_2O and CO_2 via Ceria Redox Reactions in a High-Temperature Solar Reactor, Energy Environ. Sci. 5 (2012) 6098 – 6103.

[13] S. Dey, B. S. Naidu, C. N. R. Rao, $Ln_{0.5}A_{0.5}MnO_3$ (Ln = Lanthanide, A = Ca, Sr) Perovskites Exhibiting Remarkable Performance in the Thermochemical Generation of CO and H_2 from CO_2 and H_2O, Chemistry - A European Journal 21 (2015) 7077 – 7081.

[14] Y. A. Daza, D. Maiti, R. A. Kent, V. R. Bhethanabotla, J. N. Kuhn, Isothermal Reverse Water Gas Shift Chemical Looping on $La_{0.75}Sr_{0.25}Co_{(1-Y)}Fe_YO_3$ Perovskite-type Oxides, Catalysis Today 258, Part 2 (2015) 691 – 698.

[15] J. R. Scheffe, A. Steinfeld, Oxygen Exchange Materials for Solar Thermochemical Splitting of H_2O and CO_2: A Review, Materials Today 17 (2014) 341 – 348.

[16] L. K. Rihko-Struckmann, P. Datta, M. Wenzel, K. Sundmacher, N. V. R. A. Dharanipragada, H. Poelman, V. V. Galvita, G. B. Marin, Hydrogen and Carbon Monoxide Production by Chemical Looping over Iron-Aluminium Oxides, Energy Technology 4 (2016) 304 – 313.

[17] S. Abanades, CO_2 and H_2O Reduction by Solar Thermochemical Looping Using SnO_2/SnO Redox Reactions: Thermogravimetric Analysis, International Journal of Hydrogen Energy 37 (2012) 8223 – 8231.

[18] P. G. Loutzenhiser, M. E. Galvez, I. Hischier, A. Stamatiou, A. Frei, A. Steinfeld, CO_2 Splitting via Two-Step Solar Thermochemical Cycles with Zn/ZnO and FeO/Fe_3O_4 Redox Reactions II: Kinetic Analysis, Energy & Fuels 23 (2009) 2832 – 2839.

[19] A. H. McDaniel, E. C. Miller, D. Arifin, A. Ambrosini, E. N. Coker, R. O'Hayre, W. C. Chueh, J. Tong, Sr- and Mn-Doped $LaAlO_{3-\delta}$ for Solar Thermochemical H_2 and CO Production, Energy Environ. Sci. 6 (2013) 2424 – 2428.

[20] C. L. Muhich, K. C. Weston, D. Arifin, A. H. McDaniel, C. B. Musgrave, A. W. Weimer, Extracting Kinetic Information from Complex GasSolid Reaction Data, Industrial & Engineering Chemistry Research 54 (2015) 4113 – 4122.

[21] L.-S. Fan, L. Zeng, S. Luo, Chemical-Looping Technology Platform, AIChE Journal 61 (2015) 2 – 22.

[22] X. Gao, A. Vidal, A. Bayon, R. Bader, J. Hinkley, W. Lipinski, A. Tricoli, Efficient Ceria Nanostructures for Enhanced Solar Fuel Production via High-temperature Thermochemical Redox Cycles, Journal of Material Chemistry A 4 (2016) 9614–9624.

[23] J. Zielinski, I. Zglinicka, L. Znak, Z. Kaszkur, Reduction of Fe_2O_3 With Hydrogen, Applied Catalysis A-General 381 (2010) 191 – 196.

[24] F. J. Gotor, J. M. Criado, J. Malek, N. Koga, Kinetic Analysis of Solid-State Reactions: The Universality of Master Plots for Analyzing Isothermal and Nonisothermal Experiments, The Journal of Physical Chemistry A 104 (2000) 10777 – 10782.

[25] A. Khawam, D. R. Flanagan, Solid-State Kinetic Models: Basics and Mathematical Fundamentals, The Journal of Physical Chemistry B 110 (2006) 17315 – 17328.

[26] P. Heidebrecht, V. Galvita, K. Sundmacher, An alternative method for parameter identification from temperature programmed reduction (TPR) data, Chemical Engineering Science 63 (2008) 4776 – 4788. Model-Based Experimental Analysis.